Available online at www.sciencedirect.com
SCIENCE DIRECT®
International Journal of Rock Mechanics & Mining Sciences 42 (2005) 933–949
International Journal of Rock Mechanics and Mining Sciences
www.elsevier.com/locate/ijrmms

Laboratory studies of electrical potential during rock failure

D. Eccles*, P.R. Sammonds, O.C. Clint

Mineral, Ice & Rock Physics Laboratory, Department of Earth Sciences, University College London, UK

Accepted 3 May 2005
Available online 14 July 2005

Abstract

We have investigated electrical potential and acoustic emissions signals associated with rock deformation. Five rock types were studied; Clashach, Bentheim and Darley Dale sandstones (all quartz-rich) and a Seljadur basalt and Portland limestone (both quartz-free), both air dry and the rocks were tested in distilled water. Shallow crustal conditions were simulated in a triaxial rock deformation cell with a confining pressure simulating depth of 40 MPa, pore pressures ranging 5–35 MPa, and strain rates 10^{-7}–10^{-4} s^{-1}. Precursory electric potential signals prior to failure were observed in both saturated and dry samples of the quartz-rich sandstones, but only observed in the water saturated quartz-free rocks. Co-seismic electrical signals were obtained in all tests, providing strong evidence that two of the main sources for precursory and co-seismic signals are the piezoelectric and electrokinetic phenomena. Lowering the strain rate resulted in an increase in the number of acoustic emissions. The pore volume changes during compaction and dilatancy remained approximately constant for all strain rates. Streaming potential generated by fluid flow across the sample was also measured at different stages of deformation. The potential signals increased with the pore pressure gradient.

1. Introduction

Laboratory investigations of electrical potential (EP) changes in rock have received considerable attention in recent years since it was first proposed that electrokinetic signals induced by groundwater flow could be a possible means for earthquake prediction [1]. Early experimental work on the electrokinetic effect used crushed rock samples with EP measurements (also called streaming potentials (SPs)) made as a function of pH and temperature [2–4]. These studies confirmed that the electrical double layer (EDL) model described by Overbeek [5] could be applied to rock-water systems.

Laboratory studies, including those in this study, have confirmed the existence of the electrokinetic SP signals under simulated crustal conditions of confining pressure, pore fluid pressure and deviatoric stress [6–9] and have provided useful relationships between SP parameters, such as the zeta potential, pressure, permeability, fluid concentration, flow rate, pore matrix geometry and stress state [2–4,8,10–12]. Other studies have investigated electrical conductivity, pH, valence and other influences on the EDL, including during rock deformation [13]. Laboratory studies of deformation on dry rocks without pore fluid (again including those in this study), and frictional sliding experiments have also shown that strain-induced piezoelectricity of some naturally occurring crystals can also create measurable electrical fields [7,14–17]. The effect of an applied stress on rock produces electromagnetic emissions from microscopic crack-tips [18] and if the stress state is altered sufficiently it can produce mobile electronic charges capable of producing charged surfaces even within insulating materials [19].

In laboratory triaxial experiments, the electrokinetic phenomena [2,8] and piezoelectric signals [7,17] have been investigated. The electrokinetic effect depends on many factors including grain size, permeability, surface electrical conduction, resistivity, pH, valence, size of ions and temperature with different effects depending on the heterogeneity and composition of the rock [8,20,21]. These laboratory experiments have shown that both SP and electric potential changes during deformation are

*Corresponding author. Tel.: +44 020 7679 0165.
E-mail address: d.eccles@ucl.ac.uk (D. Eccles).

1365-1609/$ - see front matter © 2005 Elsevier Ltd. All rights reserved.
doi:10.1016/j.ijrmms.2005.05.018

due to both physical and chemical effects. To increase our understanding of this and the electrokinetic effect, direct comparison of different rock types under varying conditions is required to help identify how individual rock properties affect aspects of the electrical signals recorded prior, during and after failure.

In this paper, we describe our laboratory studies using five different rock types deformed under triaxial stresses, under varying strain rates and effective pressures. The aim of this paper is to analyse streaming and electric potential changes during a full cycle of rock deformation. In particular, we have concurrently measured acoustic emissions (AE) during the triaxial rock deformation experiments, as they are highly indicative of rock deformation and failure processes [22,23]. In a companion paper [24] we explicitly investigate the role of pore fluids in the generation of electrical precursors on shear fracture.

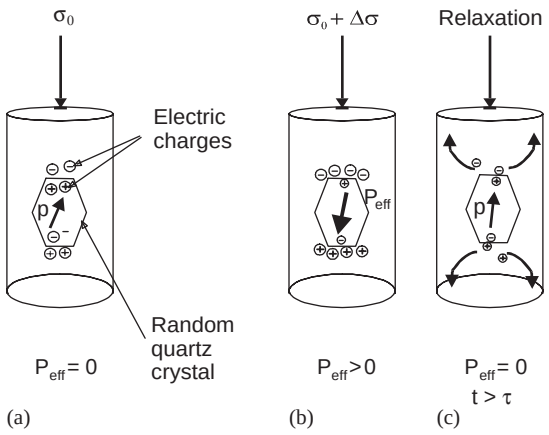

Fig. 1. Initially stress induced polarisation of quartz crystals is (a) neutralised by mobile bound charges on the charge surface. A rapid stress change (b) induces an effective polarisation in the crystal, which decays (c) through a relaxation process with time constant $\tau = \varepsilon/s$, where s is the electric conductivity; after [16].

2. Piezoelectric phenomena

A piezoelectric crystal can be defined as one that becomes electrically charged on deformation, or as one that becomes deformed when an electric field is applied. The electric polarity generated on the crystal surface is determined by the mode of deformation i.e. compression, tension or shearing. The fundamental equations describing piezoelectricity in rock samples are

$$D = \mathrm{d}\sigma + \varepsilon_{\mathrm{p}}^{\sigma} E, \tag{1}$$

$$\varepsilon = \frac{1}{C^{E}}\sigma + \mathrm{d}E, \tag{2}$$

where D is the electric polarisation, d is a matrix of piezoelectric constants, σ is the stress, ε_{p} is the permittivity, E is the electric field, ε is the strain and C is the elastic constant. From Eq. (1) it can be seen that the electrical polarisation is directly proportional to the applied stress gradient when the strain is zero.

The initial polarisation of a typical quartz crystal is neutralised by mobile bound charges in the rock (Fig. 1a) and hence a measurable EP cannot be obtained on the sample surface. With a quartz crystal in the rock that is electrically polarised in proportion to the applied stress drop, when a rapid stress drop occurs ($\Delta\sigma_{jk}$), the polarisation of the quartz crystal is reduced to

$$p_i = c_{ijk}(\sigma_{jk}^{0} - \Delta\sigma_{jk}), \tag{3}$$

where p_i is the ith component of the polarization vector and c_{ijk} is the piezoelectric modulus of the third-order tensor of the material.

The difference between the initial polarisation and the stress-induced polarisation appears as an effective polarisation (Fig. 1b). If the process occurs at a rate greater than the decay time τ for the bound charges to neutralise the effective polarisation, then this signal can be measured on the sample surface (Fig. 1c). Further details can be found in [16].

3. Electrokinetic phenomenon

The electrokinetic phenomenon involves the coupling between a fluid and a solid to produce a solid–liquid charged interface known as the EDL. The currently accepted models of the physical description were first developed in the 1910s and further modified by Stern [25], fuller accounts can be found in [2,10,26]. In a two-phase system, the four main electrokinetic effects [27] involving charge flow are (i) electro-osmosis, (ii) SP, (iii) electrophoresis and (iv) sedimentation potential. Overbeek [5] describes this solid–liquid interface as having an excess charge of one polarity ions (−Ve) compensating oppositely charged distribution of counterions (+Ve) in the nearby fluid phase, this produces the EP. The EP assumes several mechanisms; including ionisation of surface groups, adsorption of species and dipole orientation, all of these cause a charge separation. The solid–liquid boundary is composed of an inner absorbed layer and a diffuse outer layer as shown in Fig. 2 [2,4]. The rigid inner layer is made up of molecular ions in the plane of the solid surface due to the electrostatic attraction from ions in the liquid phase. Further out, the diffuse outer layer containing the counter-ionic charge density is present. These two layers are separated by a plane known as the zeta potential, which begins at the diffuse layer boundary. The value of this potential is fundamental in all electrokinetic phenomenon [28].

When a pressure gradient is introduced, the outer diffuse layer is moved in the direction of the fluid flow.

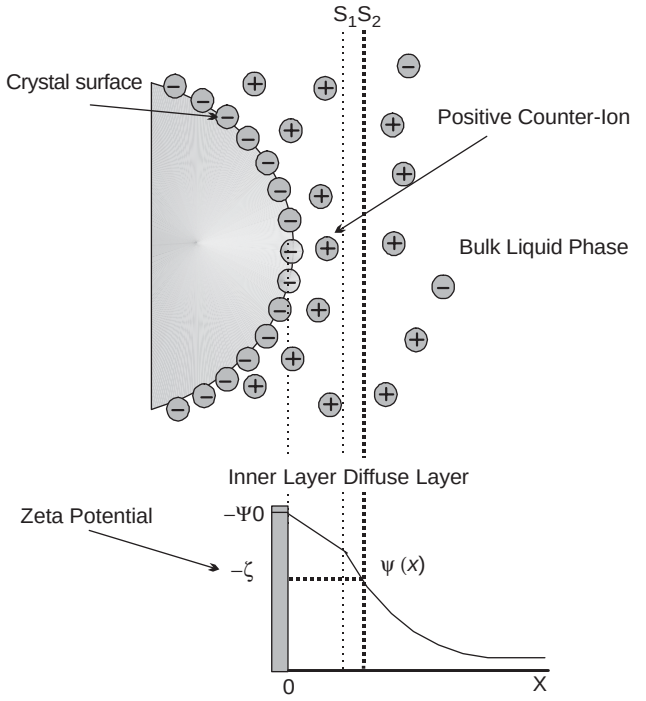

Fig. 2. Stern layer, and the variation of the potential with distance from crystal structure; after [41].

This generates an electric current, which produces an electric field causing the production of a secondary electric current opposing the primary flow. With the current taking all paths through the rock, in a steady-state situation, the two currents will be opposite and equal. The potential difference that develops between the samples ends is called the SP and can be expressed as

$$V = \frac{\varepsilon_p \zeta}{\eta(\sigma_f + (2\sum_s)/r)} P, \tag{4}$$

where $\sum_s$ is the specific surface conductance [5], ζ represent the zeta potential and η is the dynamic viscosity. The SP coupling coefficient (C_s), is defined as the ratio of SP to applied pore pressure gradient ($\Delta V/\Delta P$). Using this equation, C_s is independent of geometrical a property that is being suggested by Jouniaux and Pozzi [6], this equation could be used to interpret field data. However, studies have shown that C_s is not scale invariant but shows some permeability dependence.

The quantitative treatment of electrokinetic coupling is part of the subject of irreversible thermodynamics [29]. The coupling between electrical charge and the liquid flow can be described by

$$\begin{bmatrix} Q \\ J \end{bmatrix} = \begin{bmatrix} L_{11} & L_{12} \\ L_{21} & L_{22} \end{bmatrix} \begin{bmatrix} \nabla\varphi \\ \nabla P \end{bmatrix} \tag{5}$$

for a capillary tube where Q represents fluid flux, J is the current density, P is the fluid pressure, φ is the EP and L_{ij} represent the hydraulic coupling, electrokinetic coupling and electrical coefficients. Expanding this for current and fluid flow, the following coupled equations for porous networks are produced:

$$Q = -\frac{k}{\eta}\nabla P - \frac{\varepsilon_p \zeta}{\eta}\nabla\varphi, \tag{6}$$

$$J = -\frac{\varepsilon_p \zeta}{\eta}\nabla P - \sigma_f \nabla\varphi, \tag{7}$$

where k is the permeability, η is the fluid viscosity, ε_p is the permittivity and ζ is the zeta potential. From this it can be assumed that electric currents and SPs may be sensitive to heterogeneity in porous media [30]. Using the above equations, the induced convective current and compensating conduction current (obeying Ohms law) can be expressed as

$$J_{total} = J_{convection} + J_{conduction}. \tag{8}$$

If no external current sources are present and a steady-state system is in place ($\nabla \cdot J_{total} = 0$), then Eq. (5) can be expressed as

$$\nabla \cdot J_{conduction} = \nabla \cdot J_{convection} = S, \tag{9}$$

where S is the electrokinetic source.

4. Rock descriptions

The characteristics of the rock affect the potential signals in several ways. The composition of the sample affects the ability of the crystal to form an interface with water. Grain size is important as the smaller the grains the larger the surface area on which the EDL can operate increasing the porosity of the rock but decreasing the permeability. Permeability is important because the lower the permeability the slower fluid flow occurs during deformation and SP signals reducing the electrical signal. In order to investigate the effects of composition, grain size, permeability and porosity on the generation of the electrical signals, five rock types were chosen. Three different sandstones, with varying compositions (70–90% quartz), grain sizes (0.1–0.4 mm), a large permeability range, porosity (13–24%) and strength were used. A limestone of 18–21% porosity (similar to two of the sandstones) along with basalt was also studied, as neither have piezoelectric minerals present. A summary of the basic properties of the rocks used in this investigation is given in Table 1.

4.1. Darley Dale sandstone

Darley Dale sandstone is a Millstone Grit of Carboniferous age, stet England. It is poorly graded quartz-feldspathic sandstone bound with siliceous cement. Quartz dominates the matrix, accounting for

Table 1
Summary of rock properties

Rock types	Darley Dale sandstone	Clashach sandstone	Bentheim sandstone	Portland limestone	Seljadur basalt
Composition	75% quartz 15% clay 10% feldspar	70% quartz 10% lithic	95% quartz	100% calcium carbonate	50% pyroxene 45% plagioclase felspar
Grain size (mm)	0.008–0.8	0.3–0.4	0.1–0.5	0.25–0.50	<1
Permeability (D)	0.01	1.3	1.1	0.1	0.0000001
Porosity (%)	13–17	18–20	21–24	19–23	3
Strength (Pe = 20) (Mpa)	85	120	110	70	500

approximately 75% of the mineral content, with 10% feldspar (plagioclase and microcline) and 15% clay and other minerals forming the remainder. The grains show angular to sub-angular geometry (Fig. 3a) with grains ranging between 0.1 and 0.3 mm with only a small degree of cracking visible in some crystals. The porosity of the rock varies between 13% and 17%, and it has a permeability of about $10^{-15}\,m^{-2}$.

4.2. Clashach sandstone

Clashach sandstone is red sandstone of Permo-Triassic age and comes from Elgin (NE Scotland). The rock is composed mostly of quartz, occupying approximately 70% of the matrix, with feldspars and lithic material and other minerals forming the remainder. On average, the grains (Fig. 3b) are 0.3–0.4 mm long and appear to be well sorted with little deviation or preferred orientation and are generally sub-rounded to rounded. The porosity ranges between 15% and 20% and has a permeability of around $1.5 \times 10^{-12}\,m^{-2}$.

4.3. Bentheim sandstone

Bentheim sandstone is well-sorted quartz sandstone composed mostly of quartz crystals and held together with siliceous cement and comes from Bentheim in Belgium. Quartz accounts for approximately 95% of the rocks matrix with other minerals forming the remainder with little or no clay minerals present. The grain size (Fig. 3c) varies between 0.1 and 0.5 mm and the grains are sub-rounded in character with any undeformed crystals being relatively homogenous with little or no cracking. The porosity varies between 21% and 24% with a permeability of around $10^{-12}\,m^{-2}$.

4.4. Portland limestone

Portland is a Jurassic open textured Oolitic limestone from the Portlandian formation located in southern England. The stone is formed from micrite (fine grained calcium carbonate) ooids with small quantities of micrite present in the matrix. The shell fragments are typically 5 mm across and rounded with high porosity (18–20%) with interlinking pores giving a permeability of around $10^{-14}\,m^{-2}$.

4.5. Seljadur basalt

This basalt from Seljadur in southwest Iceland is composed of plagioclase feldspar and pyroxene with accessory minerals. This mineral composition categorises the rock as tholeitic basalt. It is a compact, high-density rock with porosity estimated at 3% and has a permeability of around $10^{-20}\,m^{-2}$.

5. Experimental apparatus and approach

To simulate shallow crustal conditions, a triaxial rock physics deformation cell was used, capable of delivering 1500 kN axial force and confining pressures up to 400 MPa. The test method is discussed by Clint and Sammonds [24]. Axial load is applied via a servo-controlled hydraulic actuator that rests on a hemispherical seat to ensure even loading of the test specimen. Different modes of operation could be achieved through the actuator, where a constant stress or strain rate could be set. Specimen deformation is measured by external linear variable displacement transducers (LVDTs).

Pore fluid pressure and volume measured at control of the rock specimen was achieved using two servo-controlled pressure intensifier systems. These intensifiers with 10 and 22 cm^3 volumes and were placed at either end of the specimen to allow for constant or changing pore pressure gradients depending on test conditions.

The cylindrical rock specimens, 100 mm long with a diameter of 40 mm (ratio of 2.5:1), were encased in a nitrile rubber stet. These jackets contain metal 12 inserts measuring both AE and EP signals. For electric potential measurements, good electrical contact between the specimen end caps and the rock specimen was required to avoid signal loss. This was achieved through the use of a thin layer of silver paint applied to the specimen ends, painted in a grid pattern and by painting the EP inserts. This improved the electrical contact,

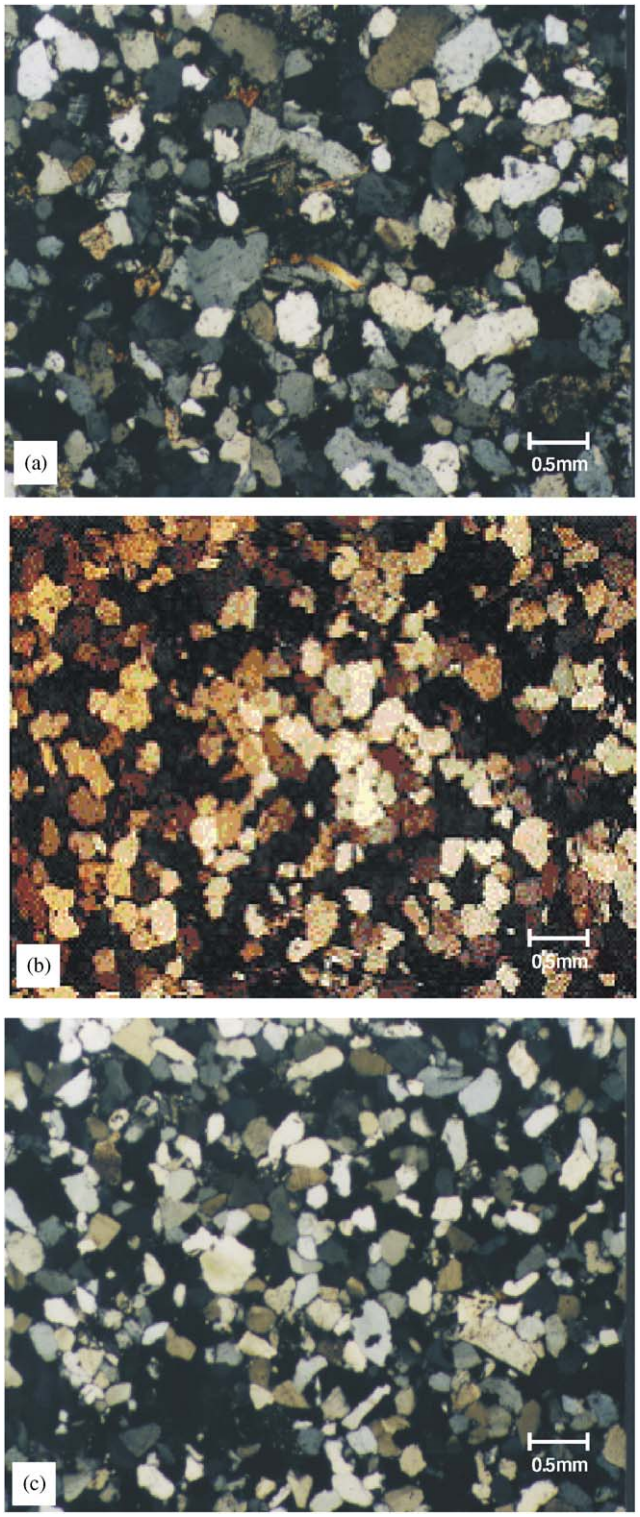

Fig. 3. Photomicrographs of (a) Darley Dale sandstone, (b) Clashach sandstone (c) Bentheim sandstone under cross-polarised light showing the mineral size and composition.

while maintaining unrestricted surface area for pore fluid flow. On either specimen end, fluid distribution plates are used to evenly disperse pore fluid to maintain saturated specimens. The jacket is held within a yoke (Fig. 4), this is

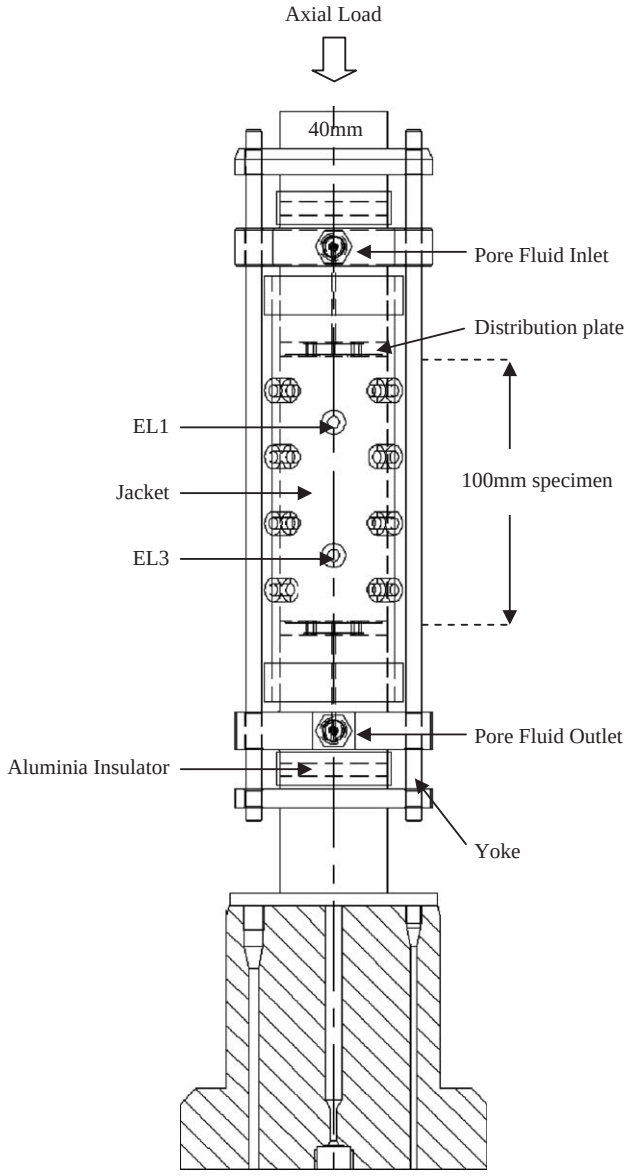

Fig. 4. Sample assembly: four electrodes of silver paint are mounted on the rock specimen, 40 mm in diameter by 100 mm long, inside the yoke.

to provide an even loading surface and allow for easy assemblage and transport of the specimen. To prevent electrical signal leaking through the bottom of the sample, an aluminia spacer is held within the yoke.

For electrical signals to be recorded, sealed lead-throughs taken through the pressure vessel end plugs were used. Each lead-through plugs contains three separate channels made up of coaxial cable with a central grounding pin [24]. Shielding of the wires allows for a total of 12 AE & EP channels to be recorded. EP signals from the rock specimens and measurements from the triaxial cell controls (load, specimen displacement, confining pressure, pore pressure, etc) were recorded by a PC logging system (Fig. 5).

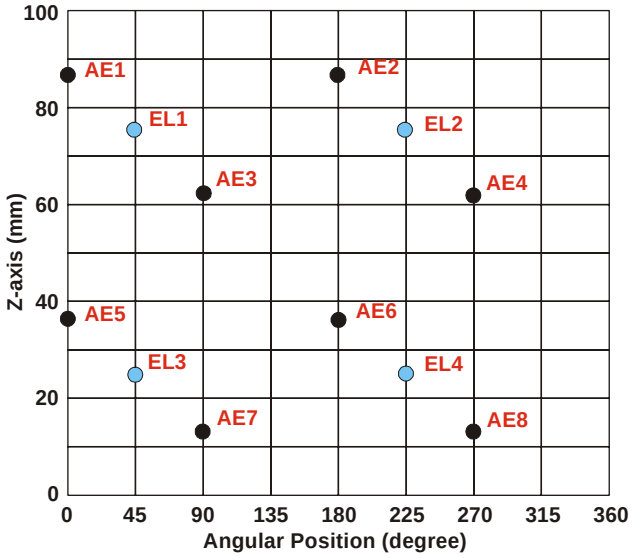

Fig. 5. Plan view of jacket with positions of AE and electrode transducers.

The AE transducers used are 1 MHz P-wave piezoelectric PZT ceramic disc 1 mm thick and 3 mm in diameter. A description of the frequency response of these transducers can be found in [31]. These transducers were attached to the stainless steel jacket inserts with conductive epoxy glue. This minimised loss of acoustic signal at the interface. The signals were amplified at 40 dB gains. The signals filtered, amplified again and passed to a calibrated Physical Acoustic LOCAN AE Analyser. The position of the AE transducers was optimised to allow AE source locations to be calculated. In our series of experiments investigating EP signals was the principal focus. So we reduced the number of AE channels to a maximum of eight. For these reasons, the source location was not investigated in this paper. Using a pulse transducer, an acoustic wave was sent to the eight transducers where it was measured.

The amplitude of the cracks can be related to the magnitude of an earthquake through the Gutenberg–Richter relationship expressed in terms of inverse cumulative frequency $N(M>m)$:

$$\log_{10}(N(M>m)) = a - bm, \tag{10}$$

where M is the earthquake magnitude. It was shown in [32], however, that the maximum likelihood estimate of the b -value from the Gutenberg–Richter form simply related to the mean magnitude $\bar{m}$ from the population

$$\frac{1}{b} = \ln 10\,(\bar{m} - m_c), \tag{11}$$

where m_c is the threshold of complete reporting. Using this equation the b-value decreases and reaches a minima coinciding with stress drop at failure. The b-value can be further used to calculate the mean crack length (MCL). In [33], the b-value was related to the fractal distribution (D) of crack lengths, and it was found that with a probability density function and a specific lower and upper bounds ($c_{\min}$, $c_{\max}$), the crack length could be calculated by

$$\langle c\rangle = c_{\min}\left(\frac{D}{D-1}\right)\left\{\frac{1-(c_{\min}/c_{\max})^{1-D}}{1-(c_{\min}/c_{\max})^{-D}}\right\} : D \neq 1, \tag{12}$$

where c is the crack length.

In order to use these equations to calculate the seismic b-value from the AE measurements and from this inferred the MCL, bins of 200 hits were used for every calculation. A program was written to calculate the b-value with a bias towards the lower amplitudes and the resulting data was fed into a MCL program. The b-value was set equal to the fractal dimension (D) and with the cumulative number of hits the MCL was calculated and normalised to the largest crack (fault) giving it a value of 1. The crack density was also calculated from the number of hits divided by rock volume for every second. A numerical threshold was chosen for both the b-value and MCL calculations to (1) normalise the experimental data to the same amplitude level and (2) prevent errors introduced through least-significant-bit noise in the a–d converter measuring the signal amplitudes. The consequence of this is that data at the bottom of the amplitude range are incompletely recorded. Under recording of events are discussed in detail by Cox and Meredith [34]. We followed the methodology of [23] and [35].

The EP signals were measured with a National Instrument (NI-6135) card using LabView software. This software-sampling rate is set at 0.5 s with an averaging function built in to remove any noise present with an accuracy of 0.01 mV. The channels were calibrated with a known voltage source. At all stages of the experiments all four electrodes were compared to identify correlations and statistically significant results relating to different parameters. Where required, an average reading was taken of the electrodes, but excluding any channel where the signal is significantly distorted relative to the other channels.

For both AE and EP results, experiments were repeated where required to confirm earlier results and identify errors present. Permeability during rock deformation was not measured in these series of experiments.

6. Experiments

6.1. Deformation testing with electric potential and acoustic emission measurements

A typical stress–time curve for the mechanical deformation of Darley Dale sandstone, taken up to dynamic failure, is shown in Fig. 6. The sample was

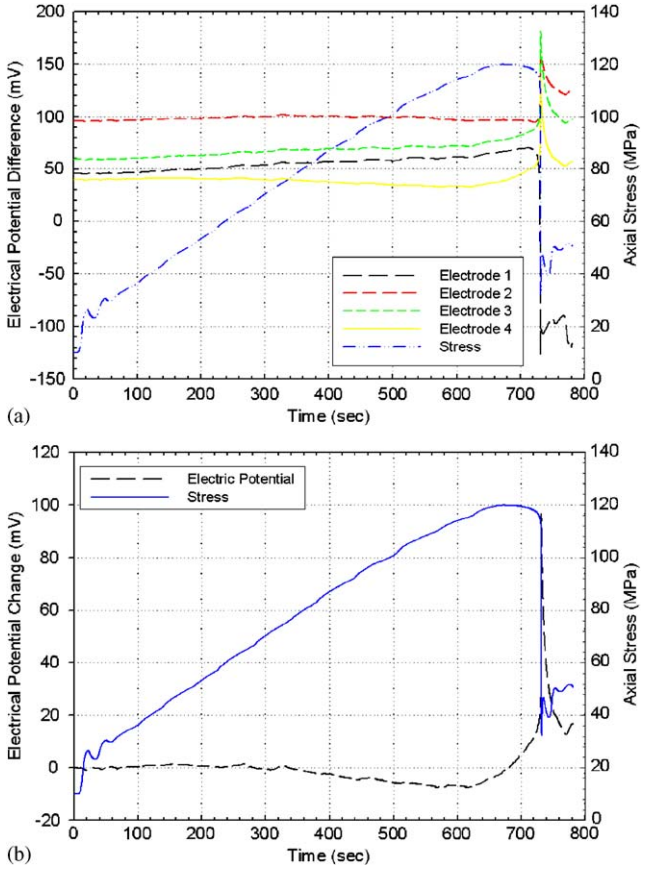

Fig. 6. Deformation cycle undertaken having a $Cp = 40\,\mathrm{MPa}$, $Pp = 20\,\mathrm{MPa}$ and strain rate of $1.5 \times 10^{-5}\,\mathrm{s}^{-1}$. Differential stress (dot–dot line) plotted against time with (a) showing the electric potential for all four electrodes and (b) electric potential change (dash line) during a deformation cycle.

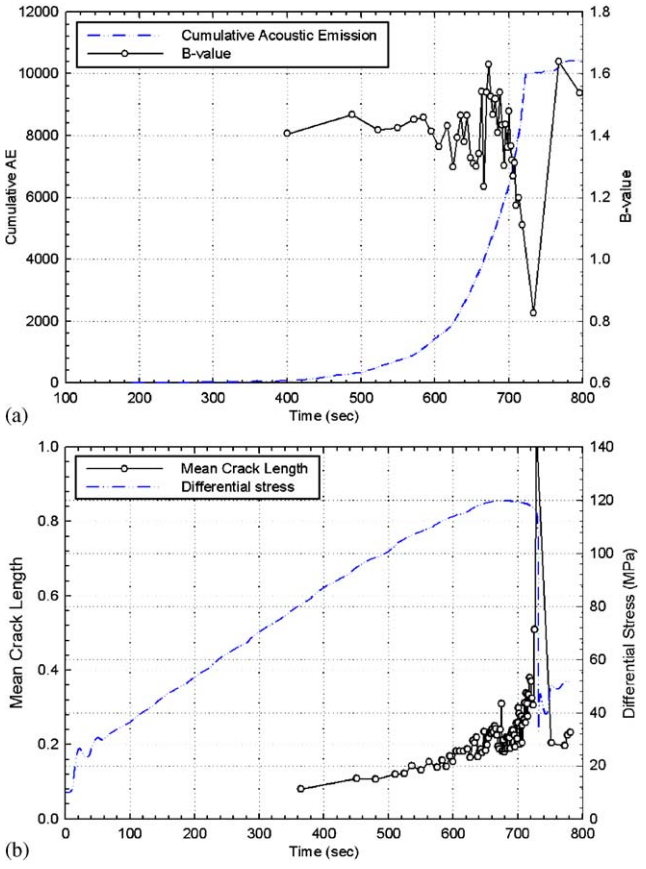

Fig. 7. Acoustic emission data (a) cumulative AE (dot–dot line) and *b*-value (circle line) against time, and (b) differential stress (dot–dot line) and normalised mean crack length (circle line) over the same experiment as shown in Fig. 6.

deformed under a confining pressure of 40 MPa and constant pore fluid pressure of 20 MPa. Fig. 6a also shows the EP differences for the four electrodes placed on the rocks specimens. As loading occurs, the EP changes, especially during the region of strain softening where the electrical signals increase, at dynamic failure a co-seismic signal (150 mV) occurs Examining the electric potential difference (Fig. 6b) the change in potentials can be seen from the decrease during dilatancy (increase in pore volume during deformation) to the rapid increase at failure of with a change of 80 mV.

In the same experiment, AE data were recorded and are plotted in Fig. 7. In Fig. 7a cumulative AE is plotted which is used to calculate the *b*-value. An increase in AE activity occurs around 60% of peak stress with AE activity increasing due to cracks beginning to open [23]. Using the *b*-value to calculate the normalised mean crack length [33] (Fig. 7b) the relationship between an increase in the stage of deformation is accompanied with an increase in crack length up to the point of failure where the largest crack (fault) occurs. Comparing the AE signals of Fig. 7b with the electric potential change during the same experiment (Fig. 6) a similar pattern in the shape of the graphs emerges.

To look at the process of deformation on the microstructure of the rock and hence on the EP signals; thin sections were taken before (Fig. 8a) and after failure (Fig. 8b) on the same-cored sample. Post-test samples were impregnated with blue epoxy resin to reveal the pore spaces and cracks. Before failure the specimen is made up of complete mineral grains that are randomly orientated and approximately equal in size with no apparent cracks present. After failure however, the structure of the sample has changed with the fault present just to the right of this thin section. Generally, 2–3 grain widths from the fault the majority of the grains show signs of cracks that are obliquely acute to the fault with preferential cracking occurring in the softer minerals with larger gaps between the new crack surfaces than in quartz. All these cracks are generally parallel and equally spaced within a single crystal but differ between crystals with some cracks extending through a couple of grains showing intra-granular and trans-granular cracking occurred during deformation.

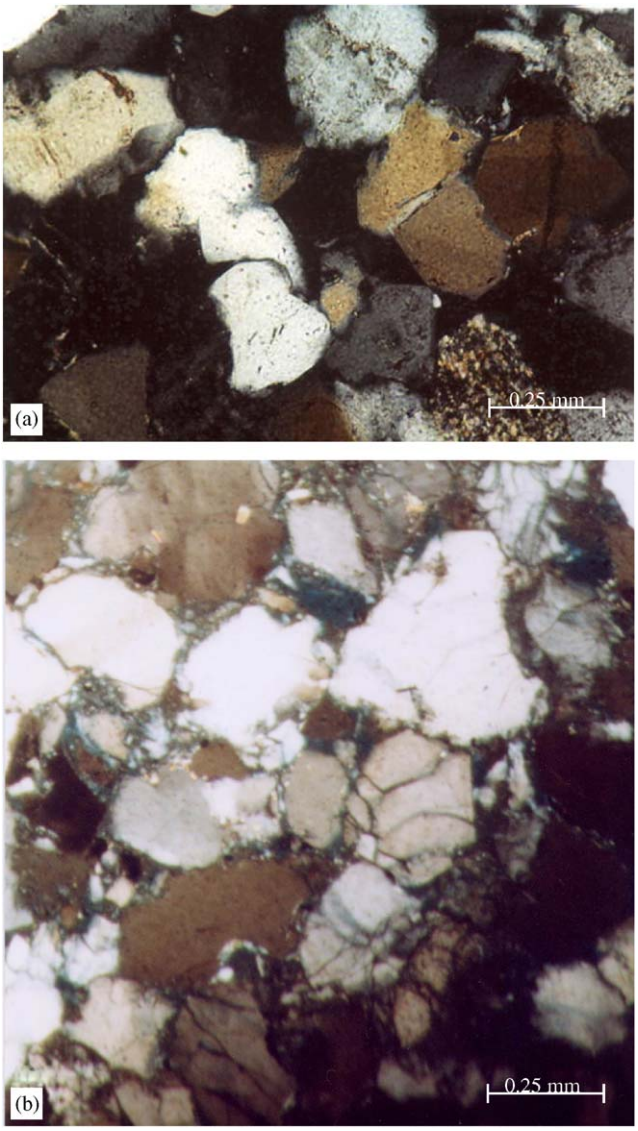

Fig. 8. Photomicrographs of Clashach sandstone in cross-polarised light (a) before deformational failure and (b) after failure showing the presence of grain cracking.

Mineral grains located further away from the fault do not have cracks running through the their centres, although cracking is present around the edges with small sections of crystal breaking off. These pieces vary greatly in size and because of their location they fill up the void space between grains. Therefore, the process of deformation which generates the AE activity comes from increasing the number of crystals to a greater number of smaller crystals; this in turn increases the pore volume of the rock but decreases the permeability by reducing the channel between grains.

6.2. Strain rate dependency

The effect of strain rate was investigated through the use of four strain rates of 1.5×10^{-4}, 1.5×10^{-5}, 1.5×10^{-6} and $1.5 \times 10^{-7}\,s^{-1}$ on Darley Dale sandstone. The influence of strain rate on AE data is shown in Fig. 9 where confining pressure was 40 MPa, pore pressure of 20 MPa with various strain rates. For the lowest strain rate less than 8000 cumulative AE hits were recorded before dynamic failure with a gentle increase in activity throughout the experiment. An increase in strain rate to 10^{-5}, the cumulative AE is a power-law curve up to dynamic failure with a total of 10,000 hits. The strain rate of 10^{-6}, the curve for the cumulative AE appears be steeper than the previous two strain rates with 11,000 hits recorded before the experiment was terminated. For all three experiments the *b*-value remains approximately constant during initial loading and decreases to a minimum of less than 0.9 when dynamic failure occurs with a corresponding decrease in the number of AE hits recorded. The electric potential signal's from the experiment done at a strain rate of $1.5 \times 10^{-7}\,s^{-1}$ is shown in Fig. 10 where the regions of compaction and dilatancy have been marked. Here, compaction is treated as a reduction in pore volume during deformation and dilatancy the region where pore volume increases up to failure. Measuring the change in EP signals during these two stages, the effect of strain rate on electrical signals can be seen with a change of 4 mV during compaction and 40 mV during dilatancy ± errors. This is repeated for the other strain rate experiments and is plotted in Fig. 11. Fig. 11a represents the change in potential signal during compaction with a change of

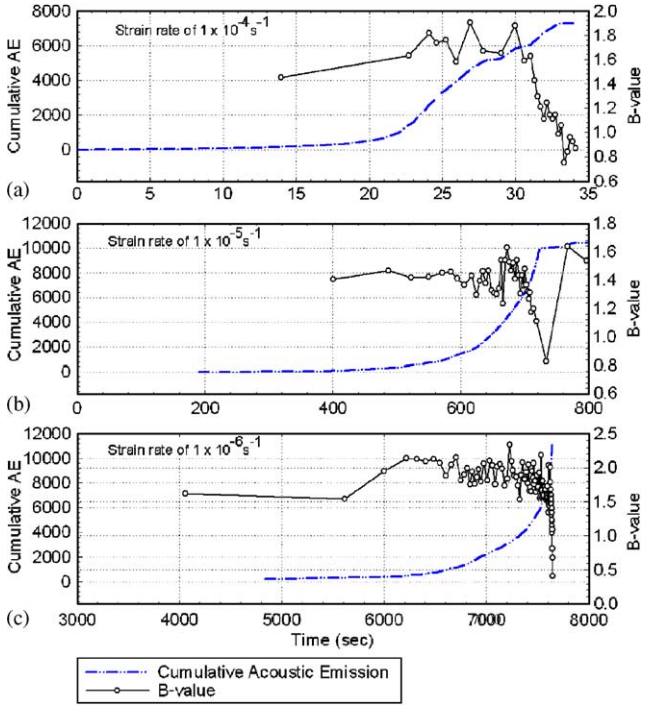

Fig. 9. Cumulative AE (dot–dot line) and *b*-value (circle line) plotted against time for strain rates of (a) $1 \times 10^{-4}\,s^{-1}$, (b) $1 \times 10^{-5}\,s^{-1}$ and (c) $1 \times 10^{-6}\,s^{-1}$ with $Cp = 40$ MPa and $Pp = 20$ MPa.

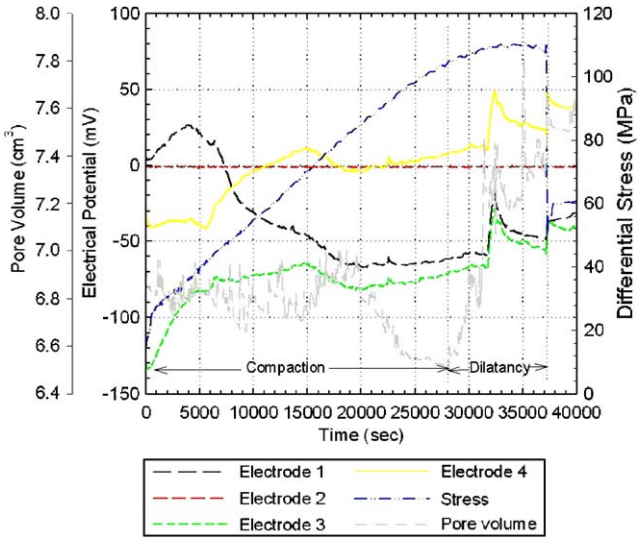

Fig. 10. Showing the regions regarded as compaction and dilatancy. Pore volume is labelled as the dot–dash line and has its axis on the far left-hand side. The other data is stress (dot–dot line) on the right-hand axis with electric potential on the left-hand axis.

25 mV for the fastest strain rate down to 4 mV for the slowest. A linear regression was applied resulting in an R^2 value of 0.9745, thus showing a good correlation between strain rate and the potential signal during the initial stage of deformation. For dilatancy shown in Fig. 11b, the electrical signals are an order of magnitude greater than those for compaction with readings of 200 mV down to 40 mV from the fastest to the slowest strain rates, respectively. A linear regression was applied, giving $R^2 = 0.9796$.

The pore volume change during compaction and dilatancy for the strain rates of 10^{-4}–$10^{-7}\,s^{-1}$ is shown in Fig. 12. For the three fastest strain rates the volume change during both stages of deformation remains constant with a change of 0.04 cm^3 during compaction compared to 0.36 cm^3 for dilatancy. For the slowest experiment the volume change is approximately twice that of the other tests.

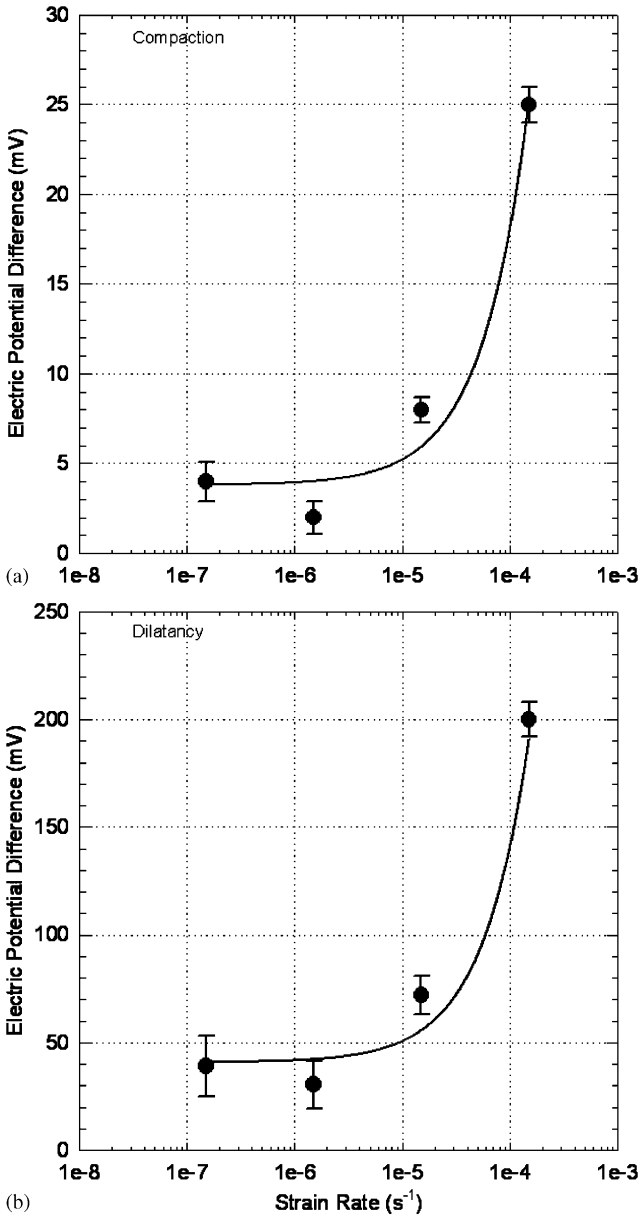

Fig. 11. Electric potential difference plotted against strain rate during (a) compaction and (b) dilitancy.

6.3. Precursory and co-seismic signals

To investigate the presence of precursory and co-seismic signals, the point of dynamic failure is studied closely during both dry (Fig. 13) and saturated (Fig. 14) experiments with quartz-rich and quarts-free specimens, Table 2 summaries these graphs. These experiments all had similar conditions with a confining pressure of 40 MPa, pore pressure of 20 MPa and a strain rate of $1.5 \times 10^{-5}\,s^{-1}$.

In Fig. 13a an almost instantaneous stress drop occurs at 15 s representing dynamic failure (time scale is arbitrary). Prior to failure all four potential signals remain fairly constant ranging from −200 mV to 250 mV. At 14 s, electrodes 1 and 3 show a increase of over 20 mV with a further increase at failure one second later of over 150 mV. For the other sandstones, precursory signal changes are visible on at least two channels with a change of around 50 mV for Bentheim and 40 mV for Clashach sandstone. In Fig. 13c, electrode 3 shows a precursory change several seconds before electrode 1. In the quartz free rocks, precursory signals are not visible, however co-seismic signals are observed of 25 and 100 mV for basalt and limestone, respectively.

With the same effective conditions as those used for the dry experiments, the results of saturated sample are

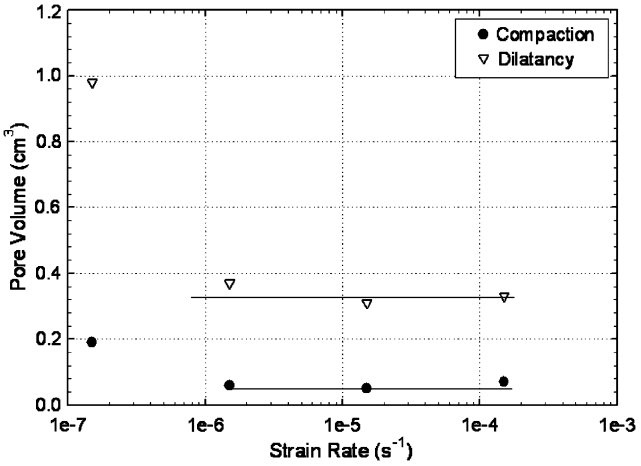

Fig. 12. Absolute pore volume change during compaction and dilatancy.

shown in Fig. 14. For both quartz-rich and quartz-free specimens a pre-seismic and co-seismic are observed. For Bentheim in Fig. 14b a precursory signal change of around 20 mV is present with a co-seismic signal change of about 50 mV. Fig. 14e shows that electrode 3 has the precursor several seconds before the other channel and is similar to that of Fig. 13c. The magnitude of the co-seismic signals differs for all specimens ranging from 20 mV in limestone to 350 mV in basalt.

6.4. SP and permeability measurements

The SP is given as the change in EP signal produced when fluid flow occurs due to the presence of a pore pressure gradient across the specimen. The SP was investigated on three sandstones (Darley Dale, Clashach and Bentheim) and a limestone (Portland) to identify differences present in the electrical signals and try to relate this to the difference in rock properties. To examine at the effect of applied pore pressure gradients on the generation of SP signals, Fig. 15 was produced. With the bottom of the sample electrically isolated, electrodes 3 and 4 are twice the distance away from the grounding point at the top of the sample compared to electrodes 1 and 2. This is seen in all three sandstones (Figs. 15a–c) where electrodes 1 and 2 are approximately half the magnitude of the other two electrodes and the increase of pore pressure gradient results in increasing potential signals with no divergence between the upper and lower electrodes. For the limestone the upper and lower electrodes diverge; the reason at present not identified. The magnitude of the SP signals generated at the maximum pressure gradient for steady-state flow for Darley Dale ($\approx$325 mV) is an order of magnitude greater than Clashach ($\approx$21 mV), which is an order of magnitude greater than Bentheim ($\approx$2 mV). Comparing this to Portland ($\approx$600 mV), the rock composition does dramatically alter the potential. Looking at the flow rate achieved for a given pressure gradient Fig. 16 shows that Clashach sandstone is more permeable than all the other specimens with a flow rate of 0.135 cm^3/s compared to 0.126, 0.01 and 0.02 cm^3/s for Bentheim, Darley Dale and Portland, respectively at a pore gradient of 25 MPa.

To examine the effect of a macroscopic fault on SP and zeta potential signals, SP was measured before and after failure as shown in Fig. 17 with adjacent schematic diagrams showing the position of the fault formed relative to the electrodes. In this figure, two dipoles, electrodes (3-1) (dipole 1) and electrodes (4-2) (dipole 2) were calculated. Before deformation, there is no significance difference between the potentials on either side of the rock sample, so the dipoles give similar readings; Darley Dale potentials going from 16 mV at 5 MPa up to 100 mV at 30 MPa compared with Bentheim going from less than 5 mV up to 14 mV and Portland with 40 mV up to 400 mV. After failure, the dipoles diverge with both dipoles giving larger magnitudes than before failure with Darley Dale giving readings of 150 and 180 mV, compared with Bentheim, which has readings of 56 and 136 mV, with dipole 2 having a larger potential than dipole 1 in both cases. From the schematic diagrams in Fig. 17 the position of the faults in both sandstone experiments are similar. For Portland however, dipole 1 is greater than dipole 2 and a change in relative position of the fault to the electrodes is observed. The zeta potential calculated from Fig. 17 is shown in Table 2.

7. Discussion

Both AE and EP signals were measured during the simulation of shallow crustal depths on various rocks including Darley Dale sandstone as shown in Fig. 6. With the onset of loading, AE and EP signals increased through the opening and closing of cracks both perpendicular and non-perpendicular to loading. The AE activity increases towards failure shown by the increase in cumulative number of hits, after failure the AE activity decreased and was solely due to frictional sliding along the fault. Using the AE activity, the *b*-value and MCL were calculated (Fig. 7) showing a possible link between AE activity and mechanical properties of the rock, this change in rock properties affects other factors including electrical signals.

For the electrodes, they share the same trend at all stages of deformation; however, due to their relative positions the signals differ slightly indicating that the rock is not behaving completely homogeneously. The photomicrographs of Clashach sandstone before and after failure (Fig. 8) show that the AE activity and potential signal can be related to cracking of minerals recorded as AE activity, which increases the surface area on which the EDL can operate.

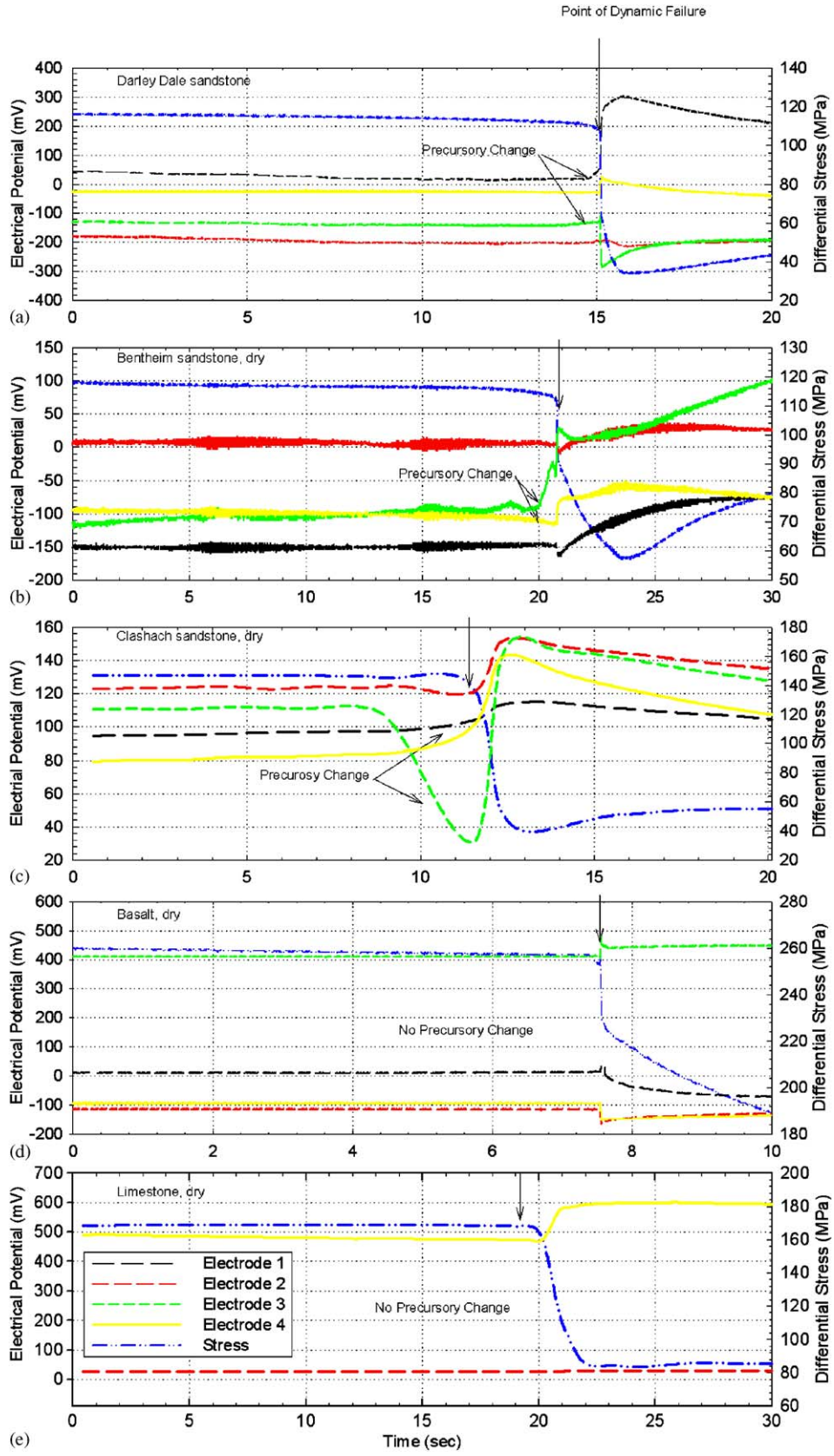

Fig. 13. The EP observed during dynamic failure of dry (a) Darley Dale sandstone, (b) Bentheim sandstone, (c) Clashach sandstone, (d) Seljadur basalt and (e) Portland limestone samples. Stress (dot–dot line) is on the right-hand axis with electric potential on the left-hand axis.

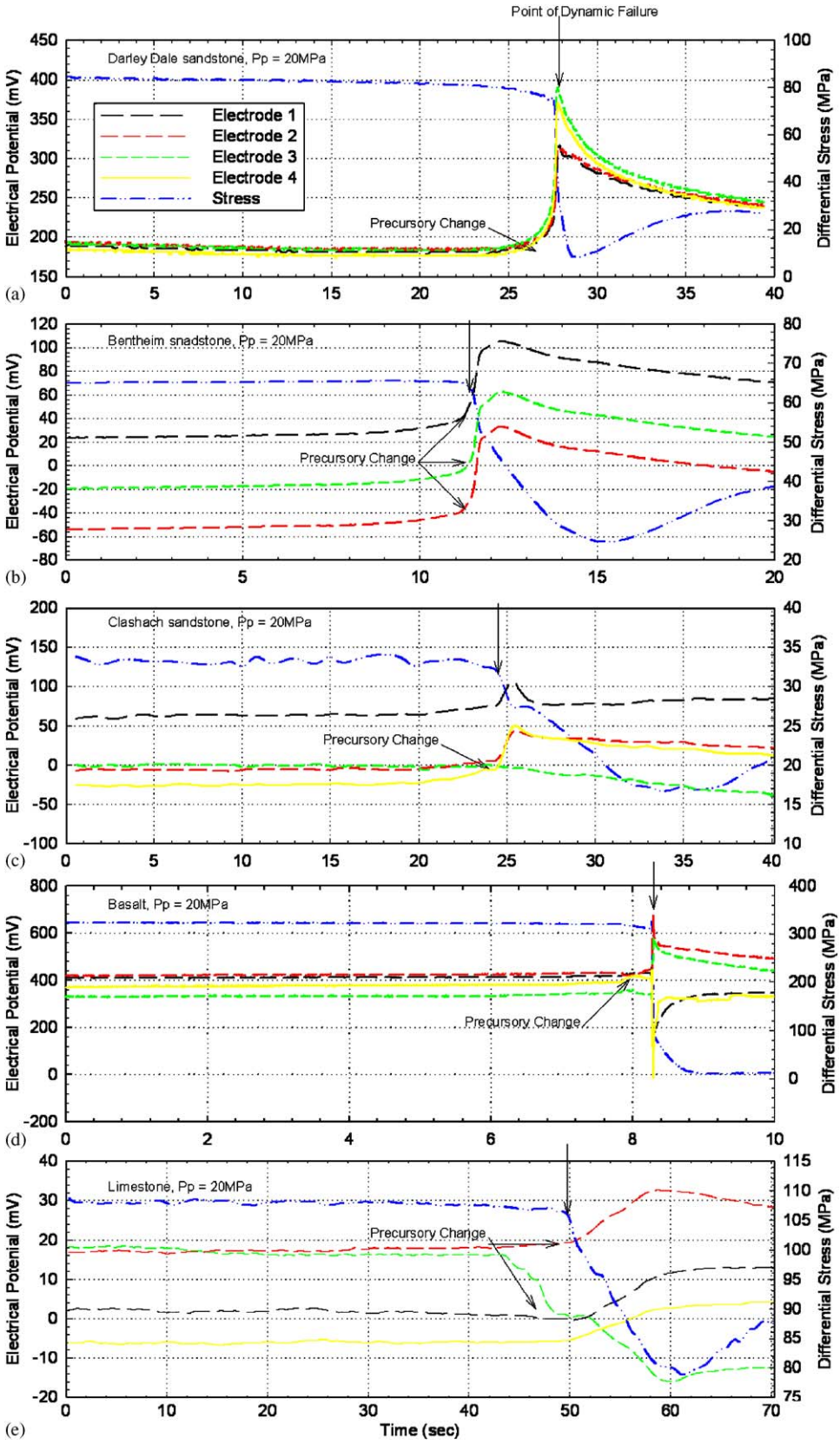

Fig. 14. The EP observed during dynamic failure of wet (a) Darley Dale sandstone, (b) Bentheim sandstone, (c) Clashach sandstone, (d) Seljadur basalt and (e) Portland limestone samples. Stress (dot–dot line) is on the right-hand axis with electric potential on the left-hand axis.

Table 2
Summary of experimental data
Crack density for Darley Dale sandstone calculated from Fig. 7

Time	Crack density
400	0.000116
450	0.000172
500	0.000327
600	0.001172
650	0.003397
700	0.002625
790	0.002935
800	0.001753

Electric potential signals around failure, values are given in mV

Rock type	Dry samples		Saturated samples	
	Pre-seismic	Co-seismic	Pre-seismic	Co-seismic
Darley Dale	27	107	100	115
Bentheim	25	40	30	65
Clashach	16	44	26	44
Icelandic	0	35	20	232
Portland	0	89	4	13

Streaming potential before and after deformation, values are given in mV

Rock type	Electrode 1	Electrode 2	Electrode 3	Electrode 4
Before failure				
Darley Dale	77.90	78.10	166.90	169.72
Bentheim	0.42	0.46	0.95	0.97
Clashach	8.56	9.49	13.37	13.78
Portland	95.51	97.72	478.39	533.67
After failure				
Darley Dale	74.30	80.40	153.20	169.95
Bentheim	4.08	2.83	7.80	6.52
Clashach	30.40	22.60	59.90	99.10
Portland	115.32	117.50	530.80	447.50

Permeability at a pressure gradient of 5 MPa before and after failure, values are given in mD

Rock type	Permeability before failure	Permeability after failure
Darley Dale sandstone	132	121
Bentheim sandstone	1067	919
Clashach sandstone	1143	1056
Portland limestone	92	67

With the formation of the fault the minerals near the failure plane are separated into several distinct parts with small gaps between the newly formed mineral surfaces of the order of a few μm and further from the fault the mineral grain edges are broken off filling the void space. This process reduces the mineral size and increase the porosity while decreasing the permeability as mentioned by Keaney [36].

In field situations, strain rates exist in the order of $10^{-12}\,s^{-1}$, these are not possible to replicate within a laboratory setting, so strain rates investigated here are much smaller and over a sufficient range that they can be scaled up. Strain rate effects are shown to be important in shear fracture [37] and frictional strength [38]. Here it has been shown that the strain rate does have an affect on the rocks strength with rock weakening occurring at high strain rates, shown by the reduced number of AE hits shown in Fig. 9. This weakening process is believed to be due to mechanical, rather than chemical effects, as the pore volume remains

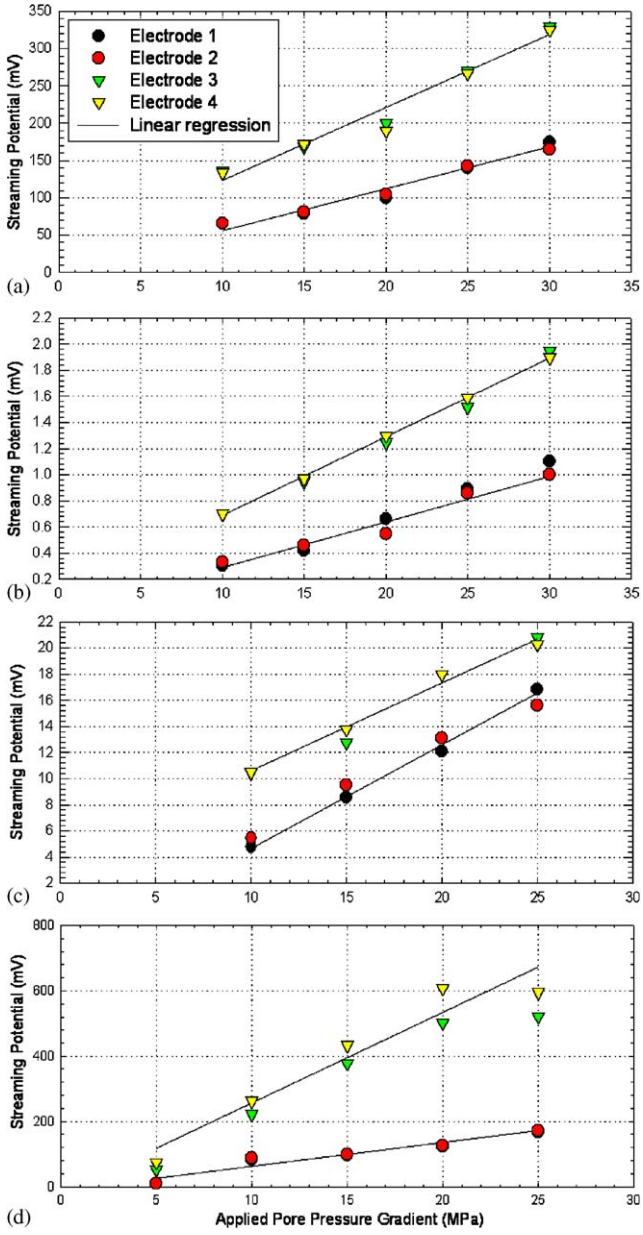

Fig. 15. SP measurements obtained at various pore pressure gradients for (a) Darley Dale sandstone, (b) Bentheim sandstone, (c) Clashach sandstone rock and (d) Portland limestone.

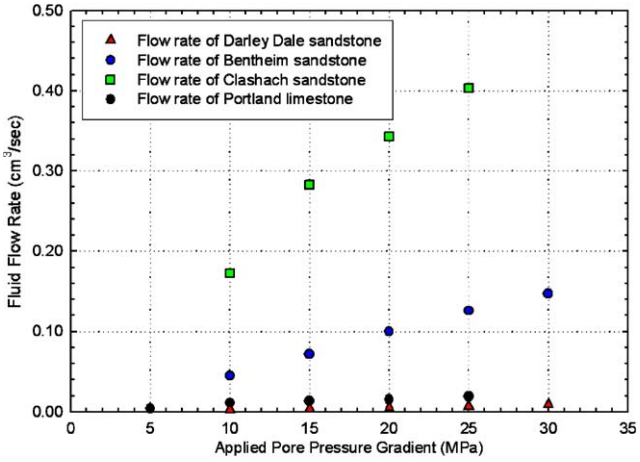

Fig. 16. Fluid flow rate of three sandstones and a limestone at various pore pressure gradients.

constant (Fig. 12). The increase of strain rate results in an increase in fluid velocity; this allows the mobile ions to enter the crystal structure and form larger electrical gradients producing increased EP signals. This is seen during compaction and dilatancy, with the latter being an order of magnitude greater because of the formation of new surface, which occurs after 70% of the peak stress. Comparing the EP signals of all the strain rates during compaction and dilatancy (Fig. 11), an equilibrium at a strain rate of 10^{-6} seems to be reached indicating that a strain rate of the order 10^{-12} would have a potential signal change only a couple of mV making it hard to identify above the background noise such as aquifers, electromagnetic changes, etc.

Around dynamic failure, precursory and co-seismic signals are generated within the rock. The mechanism for the generation of EP signals is of great interest as a possible aid to predicting earthquakes. The co-seismic signal during dynamic failure of the sandstones has been explained using the model by Yoshida et al. [16]. A previous study [15] shows that the EP signal is due to the dynamic stress drop and not the frictional slip on the fault plane although shear movement in quartz crystals is known to produce piezoelectric signals. In the quartz-rich specimens, the precursory potential signals are present due to the occurrence of the piezoelectric effect which agrees with [7]. However, another smaller process is present, generating a co-seismic signal in piezoelectric crystal free rocks of Portland limestone and Seljadur basalt that is not known. A possible explanation is that the sudden movement of the ram caused by the failure of the sample generates a change to the electromagnetism surrounding the rock and this is picked up at the electrodes; however this needs to be investigated in more detail before any firm conclusions can be determined. During deformation of the saturated specimens shown in Fig. 14, precursory and co-seismic potential signals are present in all specimens due to the electrokinetic effect [7], which shows that this phenomenon occurs in all rock types and may have greater importance than the piezoelectric effect. In the Clashach sample the fault passes through electrode 3 corresponding to an earlier precursory signal than those present in the other electrodes located some distance away from the fault. This is due to the coalescing of cracks increasing the surface area for minerals near to where the fault forms, increasing the EP signals before the other electrodes pick up the change. This is also seen in Fig. 14e, where the precursory for Portland limestone is picked up on one electrode many seconds before the others showing the

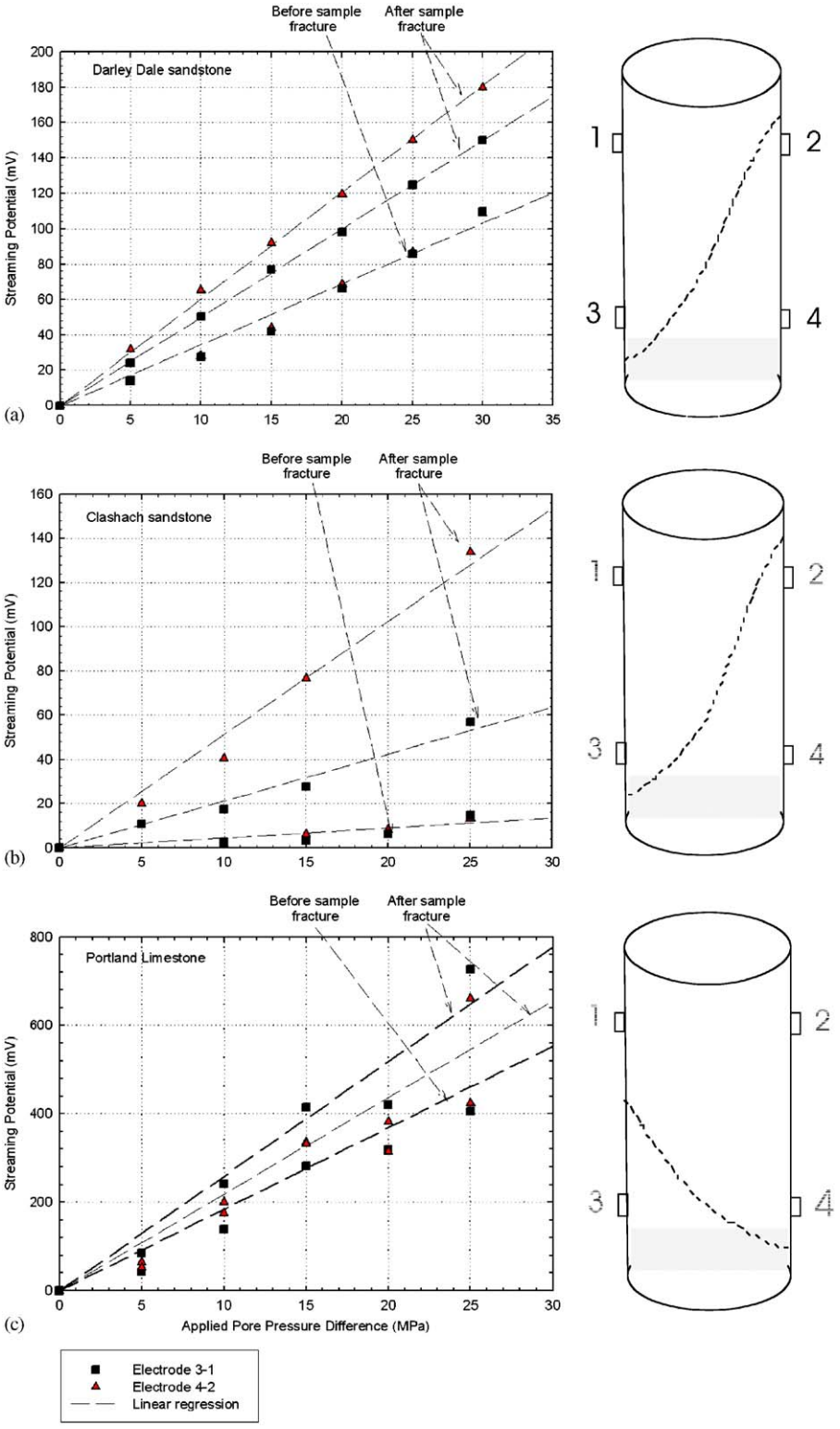

Fig. 17. SP dipoles, before and after failure for (a) Darley Dale sandstone, (b) Clashach sandstone and (c) Portland limestone.

fault is formed over time and is not instantaneous. This could potentially be used as a precursory to earthquake eruption and location if enough electrodes could be put around the failure points.

It has been proposed [39] that activation of sealed compartments would generate the pore pressure gradient [40] required to activate a fault region by causing fluid flow between the two cells which would create the

self-potential signals observed. The SP was measured along the direction of fluid flow for Darley Dale, Bentheim and Clashach sandstones and Portland limestone (details about experimental techniques can be found in [41]). SP (ΔV) has a positive correlation to the pressure gradient (ΔP), the increase in gradient also increases permeability. Depending on the flow rate, either laminar or turbulent flow occurs, which determines how the SP signals act. If the flow rate is too high, turbulent flow occurs ($Re > 15$) resulting in the conduction current unable to equilibrate with the convection current, resulting in a decrease in SP after the initial peak. In nature the fluid flow would probably be much lower than those in the laboratory setting; therefore the changes in potential would be small. SP is expected to decrease with increasing permeability [10] for a given pressure gradient but from Fig. 16, it can be seen that the flow rate is significantly different for the rock types. Here, a link between permeability and SP could not be directly established with [10] putting changes in SP due to surface conductivity rather than permeability. When dynamic failure has occurred, changes in SP depending on their relative position to the fault are observed in Fig. 17. If the fault separates the two dipoles, the dipole furthest away from the grounding point (foot wall in this case) has higher SP signals as the fault reduces the contact area between both halves of the specimen and fluid flow is altered.

Future work will concentrate on SP measurements during different stages of deformation. Different pore fluids varying in salinity (brines) will be used to investigate their effect on the SP along with temperature variations to look at its effect through thermal, chemical and mechanical interactions prior, during and after failure.

8. Conclusions

We have investigated acoustic emissions, EP and SP signals during experimental rock deformation. Both AE and EP signals are measured using a transducer array to look at the effect of strain rate, rock type on AE as well as the EP mechanism. With fluid flow occurring during deformation the effect of this on the generation of SP signals is also investigated by the use of a steady-state flow method before and after failure.

Our experiments show that in deionised water-saturated sandstone at simulated depths of 1.33 km, both AE and EP signals can be correlated to the physical mechanism during a deformation cycle. The magnitude of the EP signals observed are dependent on strain rate, which alters the physical properties of the rock including fluid velocity; this process changes the number of mobile ions formed during pore and crack closure altering the EDL's. As a result the faster the strain rate the larger the potential signal change during compaction and dilatancy.

Looking closely at the EP signals associated with dynamic failure, both precursory and co-seismic are observed being due to the piezoelectric effect in dry quartz-rich samples and electrokinetic effects in all rock specimens with different rocks having different magnitudes. Where a fault forms close to an electrode, the precursory signal is observed an extra few seconds before the other channels because of the fault forming by coalescing of cracks affects the surrounding area.

SP measurements observed through the steady-state fluid flow method show an apparent link to permeability with an increase in pressure gradient resulting in an increase in flow rate. Also the higher the pore pressure gradient, the greater the SP signals up to 30 MPa, thereafter unsteady SP occurs as convection and conductions currents created by fluid flow can no longer stay in balance. The presence of a fault further complicates the signals present as deformation changes the homogeneity of the rock to an inhomogeneous medium resulting in potential changes that can be distinguished between, depending on the relative position of the transducers to the fault.

Acknowledgements

We thank P. Meredith and A. Odedra for fruitful discussions and encouragement, and N. Hughes, S. Yoshida, J. Bowles and S. Boon for technical assistance. OCC was supported by a UK Natural Environmental Research Council grant, in collaboration with BG Group. We are grateful for this support.

References

[1] Mizutani H, Ishida T, Yokokura T, Ohnishi S. Electrokinetic phenomena associated with earthquakes. Geophys Res Lett 1976;3:365–8.
[2] Ishido T, Mizutani H. Experimental and theoretical basis of electrokinetic phenomena in rock-water systems and its applications to geophysics. J Geophys Res 1981;86:1763–75.
[3] Massenet F, Ngoc PV. Experimental and theoretical basis of self-potential phenomena in volcanic areas with reference to results obtained in Mount Etna (Sicily). Earth Planet Sci Lett 1985;73:415–29.
[4] Morgan FD, Williams ED, Madden TR. Streaming potentials properties of Westerly granite with applications. J Geophys Res 1989;94:12449–61.
[5] Overbeek JThG. Electrochemistry of the double layer, colloid science. In: Kruyt HR, editor. Irreversible systems, Vol. 1. New York: Elsevier; 1952. p. 115–93.
[6] Jouniaux L, Pozzi JP. Permeability dependence of streaming potential in rocks for various fluid conductivities. Geophys Res Lett 1995;22:485–8.
[7] Yoshida S, Clint OC, Sammonds PR. Electric potential changes prior to shear fracture in dry and saturated rocks. Geophys Res Lett 1998;25:1577–80.

[8] Lorne B, Perrier F, Avouac JP. Streaming potential measurements 1, properties of the electrical double layer from crustal samples. J Geophys Res 1999;104:17857–77.
[9] Yoshida S. Convection current generated prior to rupture in saturated rocks. J Geophys Res 2001;106:2103–20.
[10] Jouniaux L, Pozzi JP. Detection of fluid flow variations at the Nankai Trough by electric and magnetic measurements in boreholes or at the seafloor. J Geophys Res 1995;104:29293–309.
[11] Revil A, Schwaeger H, Cathles LM III, Manhardt PD. Streaming potential in porous media, 2, Theory and application to geothermal systems. J Geophys Res 1999;104(B9):20,033–48.
[12] Pengra DB, Li SX, Wong PZ. Determination of rocks properties by low-frequency AC electronics. J Geophys Res 1999;104: 29485–508.
[13] Glover PWJ, Gomez JG, Meredith PG, Boon SA, Sammonds PR, Murrell SAF. Modelling the stress/strain behaviour of saturated rocks undergoing triaxial deformation using complex electrical conductivity measurements. Surv Geophys 1996;17(3):307–30.
[14] Cres GO, Brandy BT, Rowell GA. Sources of electromagnetic radiation from fracture of rock samples in the laboratory. Geophys Res Lett 1987;14:331–4.
[15] Yoshida S, Manjgaladze P, Zilpimiani D, Ohnaka M, Nakatani M. Electromagnetic emissions associated with frictional sliding of rock. In: Hayakawa M, Fuijinawa Y, editors. Electromagnetic phenomena related to earthquake prediction. Tokyo: Terra Science; 1994. p. 307–22.
[16] Yoshida S, Uyeshima M, Nakatani M. Electric potential changes associated with slip failure of granite: preseismic and coseismic signals. J Geophys Res 1997;102(B7):14883–97.
[17] Chao LP, Huang JH. Fracture criteria for piezoelectric materials containing multiple cracks. J Appl Phys 1999;85:6695–703.
[18] Yamada I, Masuda K, Mizutani H. Electromagnetic and acoustic emission associated with rock fracture. Phys Earth Planet Inter 1989;57:157–68.
[19] Freund F, Whang EJ, Lee J. Highly mobile hole charge carriers in minerals: key to the enigmatic electrical earthquake phenomena. In: Hayakawa M, Fujinawa Y, editors. Electromagnetic phenomena related to earthquake prediction. Tokyo: Terra Science; 1994. p. 271–92.
[20] Glover PJW, Baud P, Darot M, Meredith PG, LeRavelec M, Zoussi S, Reuschle T. Alpha–beta phase transition monitored using acoustic emissions. Geophys J Int 1995;112(3):775–82.
[21] Revil A, Glover PWJ. Theory of ionic surface electrical conduction in porous media. Phys Rev B 1997;55:1757–73.
[22] Lockner DA, Byerlee JD, Kuksenko V, Ponomarev A, Sidorin A. Quasi-static fault growth and shear fracture energy in granite. Nature 1991;350:39–42.
[23] Sammonds PR, Meredith PG, Main IG. Role of pore fluids in the generation of seismic precursors to shear fracture. Nature 1992;359:228–30.
[24] Clint OC, Sammonds PR. Role of pore fluids in the generation of electrical precursors to dynamic rupture. J Geophys Res, submitted for publication.
[25] Stern O. Zűr theori der elekrolischen doppelschicht. Zeit Elekrochem 1924;30:508.
[26] Pride S. Governing equations for the coupled electromagnetics and acoustic of porous media. Phys Rev B 1994;50:15678–96.
[27] Shaw BE, Carlson JM, Langer JS. Patterns of activity preceding large earthquakes. J Geophys Res 1992;97:479–88.
[28] Mazur P, Overbeek JThG. Electro-osmosis and streaming-potentials in diaphragms, II, general quantitative relationship between electro-kinetic effects. Recl Trav Chim Pays Bas 1951;70:83–91.
[29] Overbeek JT. Thermodynamics of electrokinetic phenomena. J Colliod Sci 1953;8:420.
[30] Sill WR. Self-potential modelling from primary flows. Geophysics 1983;48(1):76–86.
[31] Read MD, Ayling MR, Meredith PG, Murrell SAF. Microcracking during triaxial deformation of porous rocks monitored by changes in rock physical properties II. Pore volumometry and acoustic emission measurements on water-saturated rocks. Int J Rock Mech Min Sci Geomech Abstr 1995;33(3):116A–7A.
[32] Aki K. Bull Earthq. Res Inst Tokyo Univ 1965;43:237–9.
[33] Main IG. A modified Griffith criterion for the evolution of damage with a fractal distribution of crack lengths: application to seismic event rates and *b*-values. Geophys J Int 1991;107:353–62.
[34] Cox SJD, Meredith PG. Microcrack formation and material softening on rock measured by monitoring acoustic emissions. Int J Rock Mech Min Sci Geomech Abstr 1993;30:11–24.
[35] Main IG, Sammonds PR, Meredith PG. Application of a modified Griffith criterion to the evolution of fractal damage during compressional rock failure. Geophys J Int 1993; 115:367–80.
[36] Keaney GM. Evolution of permeability in low porosity rocks under simulated crustal stress conditions. PhD thesis, University College London, London, 1998.
[37] Odedra A. Laboratory studies on shear fracture of granite under simulated crustal conditions. PhD thesis, University of London, London, 1998.
[38] Kato N, Yamamoto K, Yamamoto H, Hirasawa T. Strain-rate effect on frictional strength and the slip nucleation process. Tectonophysics 1992;211:269–82.
[39] Byerlee J. Model for episodic flow in high-pressure water in fault zones before earthquakes. Geology 1993;21:303–6.
[40] Sibson RH. Power dissipation and stress levels on faults in the upper crust. J Geophys Res 1980;85:6239–47.
[41] Clint OC. Electrical potential changes and acoustic emissions generated by fracture and fluid flow during experimental triaxial rock deformation. PhD thesis, University College London, London, 1999.